Soft Matter

PAPER

Aggregation behaviour of biohybrid microgels from elastin-like recombinamers†

Smriti Singh,[a] Dan Eugen Demco,*[ab] Khosrow Rahimi,[a] Radu Fechete,[b] José Carlos Rodriguez-Cabello[c] and Martin Möller*[a]

Investigation of the aggregation behavior of biohybrid microgels, which can potentially be used as drug carriers, is an important topic, because aggregation not only causes loss of activity, but also toxicity and immunogenicity. To study this effect we synthesized microgels from elastin-like recombinamers (ELRs) using the miniemulsion technique. The existence of aggregation for such biohybrid microgels at different concentrations and temperatures was studied by different methods which include dynamic light scattering (DLS), ^{1}H high-resolution magic angle sample spinning (HRMAS) NMR spectroscopy, relaxometry and diffusometry. A hysteresis effect was detected in the process of aggregation by DLS as a function of temperature that strongly depends on ELR microgel concentration. The aggregation process was further quantitatively analyzed by the concentration dependence of the ^{1}H amino-acid residue chemical shifts and microgel diffusivity measured by NMR methods using the population balance kinetic aggregation model.

Introduction

Microgels are intramolecularly cross-linked synthetic or biopolymeric chains with colloidal dimensions that can be built from a large variety of different monomers or amino acids.[1,2] The presence of the hydrophilic and hydrophobic residues along the chains as well as the possibility of making bimodal polymer chains allows precise control of their swelling behavior as a response to external stimuli such as temperature, pressure, pH, ionic strength, light and microwaves. Such microgels attract attention because of their versatility in many fields like catalysis, design of biomaterials, development of sensors, chemical separation and especially drug delivery.[2–4] Furthermore, at the fundamental level it was shown recently that relationships between the amino acid sequence and phase behavior of polypeptides provide a set of heuristics to encode lower or upper critical solution temperature in protein polymers.[5]

In the last few years biohybrid microgels have been intensively investigated mainly due to the incorporation of specific functionality originating from the biological building blocks in the synthetic microgels.[6] Many of such microgels especially

those based on polypeptide networks have the ability to undergo a volume phase transition, i.e. swelling/deswelling in response to external stimuli, such as temperature, pH, and ionic strength. This characteristic of such microgels makes them attractive candidates for applications in the field of drug delivery.[7,8]

Recently, thermo- and pH-responsive biohybrid microgels were prepared from solubilized α-elastin derived from bovine neck ligaments, by crosslinking of the lysine residues in elastin using the hydrophilic amine-reactive crosslinker poly(ethylene glycol) diglycidyl ether (PEG-DGE).[9] The aggregation process was not detected for α-elastin microgel having the concentration of 5 mg mL^{-1}. For this biohybrid microgel, information about morphological and polypeptide–water interactions in the process of reversible volume phase temperature transition (VPTT) was obtained by dynamic light scattering (DLS), ^{1}H high-resolution magic-angle sample spinning (HRMAS) NMR spectroscopy and relaxometry.[10]

Inter-protein aggregation is widely investigated mainly because of its connection to neurodegenerative diseases,[11,12] in the industrial processes for the production of therapeutic proteins as well as for the estimation of the shelf life-time of medicaments.[13,14] Such a type of aggregation is also present in recombinantly expressed human elastin polypeptides, as well as polypentapeptides and was shown to be mainly due to interactions between the hydrophobic domains.[14–18] Besides the aggregation investigation of polypeptide biopolymers, the study of this process for the synthesis of thermally responsive nanoparticles from genetically encoded peptide polymers for loading hydrophobic drugs was also reported.[19,20] A novel class of elastin like double-hydrophobic block polypeptides comprising proline-rich and

[a] DWI-Leibniz-Institute for Interactive Materials, e.V., RWTH-Aachen University, Forckenbeckstraße 50, D-52074 Aachen, Germany.
E-mail: moeller@dwi.rwth-aachen.de, demco@itmc.rwth-aachen.de;
Fax: +49-241-233-01
[b] Technical University of Cluj-Napoca, Department of Physics and Chemistry, 25 G. Baritiu Str., RO-400027, Cluj-Napoca, Romania
[c] G.I.R. Bioforge, University of Valladolid, CIBER-BBN, Valladolid 47011, Spain
† Electronic supplementary information (ESI) available. See DOI: 10.1039/c6sm00954a

glycine-rich segments have been studied showing the self-assembly of thermoresponsive nanofibers.[21]

The investigation of the aggregation behavior for the bio-hybrid microgels is an important topic because this process can cause loss of activity of biomolecules, as well as toxicity and immunogenicity. Colloids upon aggregation result in an uptake by the mononuclear phagocyte system (MPS), which is a part of the immune system. This on one hand prevents their path to the targeted tissue and on the other hand high uptake by the MPS makes MPS organs like liver and spleen main targets of oxidative stress.[22]

Hence, because of their toxic potential, aggregates can lead to an unwanted response or even overreaction of a patient's immune system. Thus to understand such behavior, in this study we use elastin-like recombinamer (ELR) microgels as a model due to well defined architecture. ELRs are genetically engineered polymers firstly designed and analyzed by Urry et al.[23] They contain natural elastin amino acidic domains and are well known for their responsive behaviour to several stimuli, namely temperature, in aqueous solution. The polymer is produced by a well established recombinant DNA technology and the recombinant nature of such polymers enables the introduction of different peptide sequences through genetic engineering to extend their properties.

Elastin-like recombinamers have special features for applications in nanotechnology and nanomedicine having well defined and totally controlled amino acid sequences.[24] To the best of our knowledge no such investigation of the aggregation process of ELR microgels has been discussed so far. A preliminary investigation on this subject was given in our previous communication.[25]

The main goal of this work is to investigate the aggregation of ELR microgels at different concentrations and temperatures. For this purpose the electron micrographs, DLS, ^{1}H HRMAS NMR spectroscopy, relaxometry and diffusometry methods are employed. The main advantage of the ^{1}H HRMAS technique is related to the possibility of accessing information about the behavior of hydrophobic and hydrophilic amino acid side chains. The coacervation process is quantitatively analyzed by the concentration dependence of the ^{1}H residue chemical shifts and microgel diffusivity is measured by NMR methods using the population balance kinetic aggregation model.

Materials and methods

ELR microgel synthesis

Elastin like recombinamer (ELR) 3KV84: ABBBBBB (M_w = 35 085 g mol^{-1}), where A = MGKKKP and B = (VPGVG)$_{14}$ was obtained from Prof. José Carlos Rodriguez-Cabello as a salt free lyophilized powder. Data on its production and characterization can be found elsewhere.[26] The crosslinker poly(ethylene glycol) diglycidyl ether PEG-DGE (M_w = 526 g mol^{-1}) was purchased from Sigma Aldrich (Germany). n-Hexane (99%, VWR), Span 80 (Sigma), Tween 80 (Sigma), and tetrahydrofuran (99% Sigma Aldrich) were used as received. Dialysis membranes

(molecular weight cut-off 100 kDa) were purchased from Spectrum Laboratories.

ELR microgels were prepared by the inverse mini-emulsion method with molar ratios of recombinant elastin polypeptide to crosslinker of 1 : 1. For the synthesis of the microgels 25 mg (7.125 × 10^{-4} mmol) of ELR polypeptide was dissolved in 125 µL of 0.04 M PBS buffer (pH 9) and dispersed in 1.25 mL of n-hexane containing 37.5 mg of surfactant (3 : 1 weight ratio of Span 80 and Tween 80). Subsequently, the dispersion was ultrasonicated under ice cooling for 60 s using a Branson sonifier W450 with a $\frac{1}{4}$ inch diameter horn, at a duty cycle of 30% and output control of 90%. Crosslinking was affected by the addition of PEG-DGE (5.344 × 10^{-4} mmol, w.r.t, 3 lysine in the elastin polypeptide) followed by further sonication for another 60 s. The dispersion was further agitated for 45 min at room temperature before the reaction was quenched by the addition of 1.5 mL of HCl (1.0 mM). Separation of the microgels was achieved by centrifugation at 10 000 rpm for 30 min with subsequent decantation of the supernatant. Microgels present in the aqueous solution were carefully washed with hexane (2 × 1.5 mL) and THF (4 × 2.5 mL) in order to remove the surfactants and unreacted ELR. The remaining organic solvents and acid were removed by dialysis. Purified microgels were stored in Millipore water at −15 °C for further use. Furthermore, to avoid problems with the history of the samples, fresh ELR microgels were prepared for analysis if the storage was longer than one month.

Cryo-field emission scanning electron microscopy (Cryo-FESEM)

Electron micrographs of ELR microgels with the PEG-DGE cross-linker with a molar ratio of 1 : 1 were obtained using field emission scanning electron microscopy (HITACHI S-4800 instrument) in a cryo-mode. For the measurements an aqueous solution of microgels with a concentration of 10 mg mL^{-1} was used. The secondary electron images have the resolution of 1.0 nm using a 1 kV accelerating electron beam. The sample was fixed on a holder and was rapidly frozen with boiling liquid nitrogen at −220 °C. It was then transferred to the high-vacuum cryo-unit, the Balzer BF type freeze etching chamber. The cryo-chamber equipped with a knife can be handled from outside by means of a lever to fracture the sample at a temperature of −145 °C by which imaging of the surface of inner morphology was aimed. The sample was sublimated for 10 min at −95 °C in order to remove the residual water. Then the entire sample was further inserted into the observation electron microscope chamber.

Cryo-transmission electron microscopy (Cryo-TEM)

TEM micrographs were taken on a Carl Zeiss Libra™ 120 Microscope (Oberkochen, Germany). The electron beam accelerating voltage was set at 120 kV. The TEM grid was hydrophilized in a plasma oven for 90 seconds before use. A drop of the sample was trickled on a piece of carbon-coated copper grid. Cryogenic TEM samples were prepared by rapid vitrification from aqueous dispersion using a plasma-treated lacey grid and a vitrobot system. For grey value analysis of the cryo-TEM images the software "Image J" (version 1.46τ) was used.

Dynamic light scattering (DLS)

Microgel solutions of 2 mg mL^{-1} and 10 mg mL^{-1} in double-distilled water were passed through a 5 μm poly(tetrafluoro-ethylene) membrane filter. Microgel sizes were determined by photon correlation spectroscopy performed at the scattering angle of $\theta = 90°$ with a setup consisting of an ALV-SP2 goniometer, an ALV-SIPC photomultiplier, a multiple τ digital real-time AVL-7004 correlator, and a solid-state laser (Koheras) with a wavelength $\lambda = 473$ nm. The temperature range of 20–55 °C was used for testing the hysteresis of the hydrodynamic radius (R_h). The toluene bath temperature was controlled to a precision of ±0.1 °C. For individual dynamic light scattering measurements in the heating and cooling mode, individual data were collected for 180 s, with the temperature steps of 3 °C. At each temperature an equilibration time of 10 or 45 minutes was allowed. The vat of toluene matched the index of refraction of the glass cells. The dispersions were sufficiently dilute to diminish multiple scattering. At each temperature five data were taken and the average from these measurements was presented.

Proton high-resolution magic angle sample spinning (HRMAS) spectroscopy, relaxometry, and diffusometry

For proton high-resolution magic-angle sample spinning (HRMAS) NMR spectra, ELR microgels with a molar ratio of 1 : 1 to the crosslinker was used at different concentrations ranging from 2 mg mL^{-1} to 10 mg mL^{-1} in D$_2$O and measured at various temperatures in the range of 15–55 °C. For this purpose a wide-bore AV700 Bruker NMR spectrometer operating at 700.2378 MHz was used. A cross-polarization MAS probe with a 3.2 mm rotor was employed at the rotor frequency of 5 kHz. The temperature was maintained within ±0.5° K using a Bruker temperature control unit. All the ^{1}H HRMAS spectra were externally referenced to TMS. For all measurements the recycle delay was 7 s, the radio-frequency pulse length was 1.9 μs, while the dwell time was 10 μs, and the number of scans was 64. The time domain data were 4k and the zero filling was done with 16k.

The sensitivity of the analysis to the aggregation and volume transition is increased by using ^{1}H HRMAS spectra encoded by the transverse relaxation and edited by the spin echo. The pulse sequence is $90°_x – \tau – 180°_y – \tau – spin echo – t$ (acquisition), where $90°_x$ and $180°_y$ are radio-frequency pulses with the flip angles of 90° and 180° having phases of x and y in the rotating reference frame. The interpulse time is $\tau = 10$ μs, the encoding time is 2τ and the free induction decay is detected for the duration t. The relative spectral integral intensities of the ^{1}H HRMAS spectra were measured using TopSpin 3.2 Bruker software. The sample size placed in a MAS 3.2 mm rotor is about 5 mm and the volume used is 15 μL. The stability of the temperature together with that of the magnetic field of high strength (1 ppm = 700 Hz), good field shimming, and intrinsic narrow resonances allows us to measure reproducible chemical shifts with the estimated standard deviation of 2% over 24 hours.

The microgel aggregate diffusivities were measured using the same AV700 Bruker NMR wide bore spectrometer equipped

with a Diff50 Bruker unit. A pulsed-field-gradient stimulated echo (PFGSE) sequence of Stejskal–Tanner[27] was used. The experiment is two-dimensional, by recording the spectral peak evolution under the applied field gradient. The delays were set to $\delta = 1$ ms and $\Delta = 40$ ms. A field gradient g in the z direction was applied, incremented in 32 steps from 5% to 95% with a maximum field gradient of 30 T m^{-1}.

Theory

Concentration dependence of amino acid side chain chemical shifts by population balance kinetic and isodesmic aggregation models

In order to model the aggregation of ELP microgels at the early stages we shall consider in the following a microgel denoted by N (hereafter a native unimer or native monomer) that aggregates reversibly into two microgels denoted by D (hereafter called dimers). The aggregation process is reversible[12] and well described by a modified Lumry–Eyring model,[28] which includes the denaturation of microgel followed by the reversible formation of dimers. The kinetic scheme for the aggregation process at the early stages, neglecting the formation of trimers and high-order i-mers (see below), is shown in Scheme 1.

The equilibrium constant for the formation of the reversible reactive intermediate is denoted by K_{eq} and the forward and backward coacervation rate constants for dimers are k_1 and k_{-1}, respectively. For the concentration of reactive species we can write[12,28]

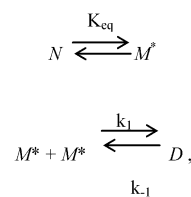$$[M^*] = \frac{K_{eq}}{1 + K_{eq}}[M], \tag{1}$$

where $[M] = [N] + [M^*]$ is the total unimer concentration that is a measurable quantity.

The time evolution of the unimer and dimer concentrations in the process of aggregation is given by the population balance kinetic equations[29,30]

$$\frac{d[M]}{dt} = -2k_1^{app}[M]^2 + 2k_{-1}[D]$$

$$\frac{d[D]}{dt} = k_1^{app}[M]^2 - k_{-1}[D], \tag{2}$$

where the forward apparent rate constant is

$$k_1^{app} \equiv \left(\frac{K_{eq}}{1 + K_{eq}}\right)^2 k_1. \tag{3}$$

$$N \underset{}{\overset{K_{eq}}{\rightleftharpoons}} M^*$$

$$M^* + M^* \underset{k_{-1}}{\overset{k_1}{\rightleftharpoons}} D,$$

Scheme 1 The reversible kinetic reactions for the formation of reactive microgel (M*) from the native unimer (N) and the aggregated microgel (dimer D).

In the kinetic eqn (2) monomer–oligomer aggregation rates were neglected. The conservation of the total number of unimers having the concentration $[M_0]$ allows us to write,

$$[M(t)] + 2[D(t)] = [M_0], \tag{4}$$

where $[M(t=0)] = [M_0]$, $[D(t=0)] = 0$, and $d[M(t)]/dt + 2d[D(t)]/dt = 0$. The last equation is satisfied by eqn (2).

The analytical solution for instantaneous unimer concentration $[M(t)]$ of the coupled nonlinear differential eqn (2) is given by

$$[M(t)] = \frac{(A-B)C + AE\exp(\Delta^{1/2}t)}{C + E\exp(\Delta^{1/2}t)}, \tag{5}$$

where the parameters A, B, C, and E are defined by

$$A \equiv \frac{\Delta^{1/2} - k_{-1}}{4k_1^{\text{app}}}, B \equiv \frac{\Delta^{1/2}}{2k_1^{\text{app}}},$$

$$C \equiv \Delta^{1/2} - 4k_1^{\text{app}}[M_0] - k_{-1}, \tag{6}$$

$$E \equiv \Delta^{1/2} + 4k_1^{\text{app}}[M_0] + k_{-1}$$

and

$$\Delta \equiv k_{-1}^2 + 2k_{-1}k_1^{\text{app}}[M_0]. \tag{7}$$

The observed equilibrium NMR chemical shift of the aggregated species denoted by δ_{obs} can be evaluated in the approximation of the isodesmic model,[30,31] by the relationship

$$\delta_{\text{obs}} = \frac{[M]_{\text{eq}}\delta_m + 2[D]_{\text{eq}}\delta_d}{[M_0]}, \tag{8}$$

where δ_m and δ_d are the chemical shifts of the unimer and the dimer, respectively. This type of isodesmic reaction is often used as a hypothetical reaction and such processes have the advantages for theoretical treatment. The equilibrium concentration $[M]_{\text{eq}}$ and $[D]_{\text{eq}}$ reached for the ensemble of microgels at the beginning of the NMR experiments can be evaluated from eqn (4) and (5) in the limit of long times compared to the inverse of the kinetic rates. We obtain finally,

$$[M]_{\text{eq}} = A, \text{ and } [D]_{\text{eq}} = \frac{[M_0] - A}{2}. \tag{9}$$

Eqn (8) is valid if the dimerization process that is considered partially reversible, being faster compared to the time window of the NMR measurement time.

The final relationship for the observed chemical shift of the microgels involved in the aggregation process can be obtained from eqn (8) and (9)

$$\delta_{\text{obs}} = \frac{\left(k_{-1}^2 + 2k_{-1}k_1^{\text{app}}[M_0]\right)^{1/2} - k_{-1}}{4k_1^{\text{app}}[M_0]}\delta_m$$
$$+ \left\{1 - \frac{\left(k_{-1}^2 + 2k_{-1}k_1^{\text{app}}[M_0]\right)^{1/2} - k_{-1}}{4k_1^{\text{app}}[M_0]}\right\}\delta_d. \tag{10}$$

The above equation is formally identical to that obtained from the original isodesmic model[31] if the effective aggregation constant K_{eff} is defined by $K_{\text{eff}}c = 2(k_1^{\text{app}}/k_{-1})[M_0]$, where c is the initial concentration of microgels $[M_0]$. Hence, K_{eff} contains information about the rate constants of the reversible aggregation process of dimers. Finally, we can write

$$\delta_{\text{obs}} = \left(\frac{\sqrt{1 + K_{\text{eff}}c} - 1}{2K_{\text{eff}}c}\right)\delta_m + \left(1 + \frac{1 - \sqrt{1 + K_{\text{eff}}c}}{2K_{\text{eff}}c}\right)\delta_d, \tag{11}$$

Using eqn (11) from the fit of the observed chemical shift δ_{obs} for amino acid side chains NMR resonances in the ^{1}H HRMAS spectrum measured as a function of microgel concentration we can obtain the values for δ_m, δ_d, and microgel effective aggregation constant K_{eff}.

In the above model that describes the effect of microgel aggregation on the observed chemical shift the existence of a dynamic equilibrium concentration for the dimers is supposed to be present in the time window of the NMR experiment that was established before the experiment starts. Furthermore, the concentration of the species like trimers, *etc.* are considered to be small compared to those of monomers and dimers and hence is neglected. This is assisted by the microgel size statistics measured by cryo-FESEM micrographs (Fig. 2b). In the approximation of dimer aggregates using the hybrid model of the population balance kinetic approach and isodesmic theory only the ratio of the rate kinetic constants k_1^{app}/k_{-1} can be measured. It can be stated that the average chemical shift δ_{obs} as well as δ_m and δ_d can be measured for hydrophobic and hydrophilic amino acid side chains of ELR microgels and show different sensitivities to the biohybrid microgel conformational changes due to aggregation (*vide infra*).

Concentration dependence of ELR microgel diffusivity by population balance kinetic and isodesmic hybrid models

In the limit of fast exchange between unimers and dimers on the time scale of self-diffusion NMR measurements[31,32] the measured average diffusivity (D_{meas}) is given by

$$D_{\text{meas}} = \frac{[M]_{\text{eq}}D_m + 2[D]_{\text{eq}}D_d}{[M_0]}, \tag{12}$$

where D_m and D_d are self-diffusion coefficients of unimers and dimers, respectively. We mention that the microgel species are in a state of dynamic equilibrium reached at the beginning of the diffusion experiment. Under these assumptions, from eqn (6), (7), (9), and (12) we can write

$$D_{\text{meas}} = \left(\frac{\sqrt{1 + K_{\text{eff}}c} - 1}{2K_{\text{eff}}c}\right)D_m + \left(1 + \frac{1 - \sqrt{1 + K_{\text{eff}}c}}{2K_{\text{eff}}c}\right)D_d, \tag{13}$$

where $K_{\text{eff}} = 2(k_1^{\text{app}}/k_{-1})$. The fit of the measured effective diffusivity of microgels as a function of microgel concentration c at a fixed temperature leads to the individual diffusivities D_m and D_d and effective aggregation constant K_{eff}. The biohybrid microgel diffusivities D_m and D_d assumes infinite dilution of particles in the absence of any inter-microgel interactions.[33]

A more specific form of eqn (13) can be obtained using the hydrodynamic models, where the ratio D_d/D_m is given by

$$\frac{D_d}{D_m} = (2)^{-1/3}F_2, \qquad (14)$$

where F_2 is a geometrical factor.[34,35] An average value of $F_2 = 0.731$ for dimer formation was proposed in ref. 36.

The microgel dimers to some approximation can be considered as rigid rod like particles with the aspect ratio $p = L/d$, where L is the length and d is the average diameter of the rod like dimer. The translational diffusion coefficient has been computed using the bead–shell model[36] and is given by

$$D_d = \frac{k_B T(\ln p + C_t)}{3\pi\eta_0 L}, \qquad (15)$$

where k_B is the Boltzmann constant, T is the absolute temperature, and η_0 is the viscosity of the solvent. In eqn (15) the end-effect term C_t is expressed by interpolating the equation[36–38]

$$C_t = 0.312 + \frac{0.565}{p} + \frac{0.100}{p^2}. \qquad (16)$$

We shall note at this point that a dumbbell that consists of two spheres of radius a having the distance between their centers L is a better model for microgel dimers. For such a case an asymptotic result similar to eqn (16) can be derived[38] that describes accurately the term C_t only for $L/a > 10$. This is non-realistic for the microgel dimers shown by cryo-TEM in Fig. 1c. Hence, we will use the simplified approximation of cylinders described using eqn (15) and (16).

Another effect that reduces the value of particle diffusivities is related to the process of crowding or self-obstruction.[39–41] This effect is complicated by the many-body problem and only approximation of the reduction factor that depends on the particle concentration was discussed.[40–42] Furthermore, none of the crowding models account for the presence of the aggregation process. The reduction of the self-diffusion coefficient of globular proteins due to the crowding effect can be described using the Smoluchowski equation in the low dilute limit,[40]

$$D_{cr} = D_m(1 - \lambda c), \qquad (17)$$

where the constant λ depends on interparticle interactions.[42] The combined effect of aggregation and crowding can be described using eqn (13) and (17) by the relationship

$$D_{meas} = \left(1 + \frac{\sqrt{1 + K_{eff}c} - 1}{2K_{eff}c} - \lambda c\right)D_m$$
$$+ \left(1 + \frac{1 - \sqrt{1 + K_{eff}c}}{2K_{eff}c}\right)D_d. \qquad (18)$$

The above equation can be simplified using eqn (14) and the average value of $F_2 = 0.731$ for dimer formation[35] which leads to $D_d = 0.58D_m$. We finally write

$$D_{meas} = \left(\frac{a\sqrt{1 + K_{eff}c} - 1}{K_{eff}c} - \lambda c + b\right)D_m, \qquad (19)$$
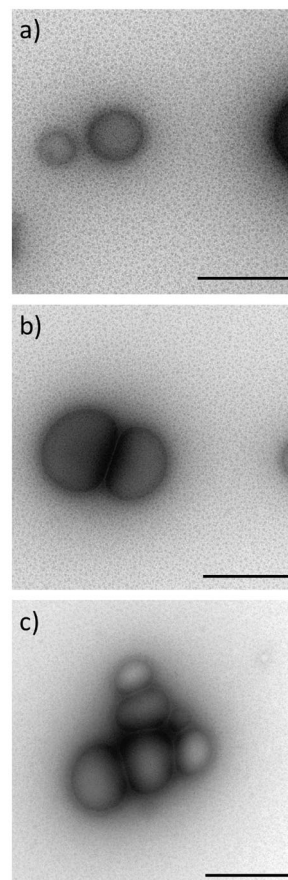
where $a = 0.21$ and $b = 1.58$.

Fig. 1 Cryo-TEM pictures of ELR microgels with a concentration of 10 mg mL^{-1} after incubation for 5 h at 60 °C. The coacervation of unimers in dimers for the incipient stage of the process is shown in (a), scale 500 nm, and the fused dimers is shown in (b), scale 500 nm. The presence of multimers is shown in (c), scale 500 nm.

Results and discussion

Cryo-TEM and cryo-FESEM micrographs

The ELR microgel aggregation is visible from cryo-TEM and cryo-FESEM micrographs. The formation of different multimers in the aggregation process is shown in Fig. 1a–c. Similar results for unimers and dimers were reported in our communication given in ref. 25. The micrographs reported in the present work were obtained by cryo-TEM using a sample with a concentration of 10 mg mL^{-1} incubated at 60 °C for 5 h. The incipient stage of coacervation is shown in Fig. 1a and the formation of a dimer is shown in Fig. 1b. The existence of a limited number of multimers is also revealed (Fig. 1c).

From the cryo-FESEM images it could be clearly seen that after heating at 60 °C for 5 h the sample of ELR microgels starts to aggregate (Fig. 2a). Based on several micrographs (Fig. 2a, one out of many), the statistics of the i-mers is shown in Fig. 2b. For this incubation temperature and time the unimers and dimmers dominate the ELR microgels. The number of trimers per µm^2 represents about 11% from the total amount of unimers and dimmers in the imaged area. Cryo-FESEM micrographs of ELR microgel with a concentration of 2 mg mL^{-1} in water incubated
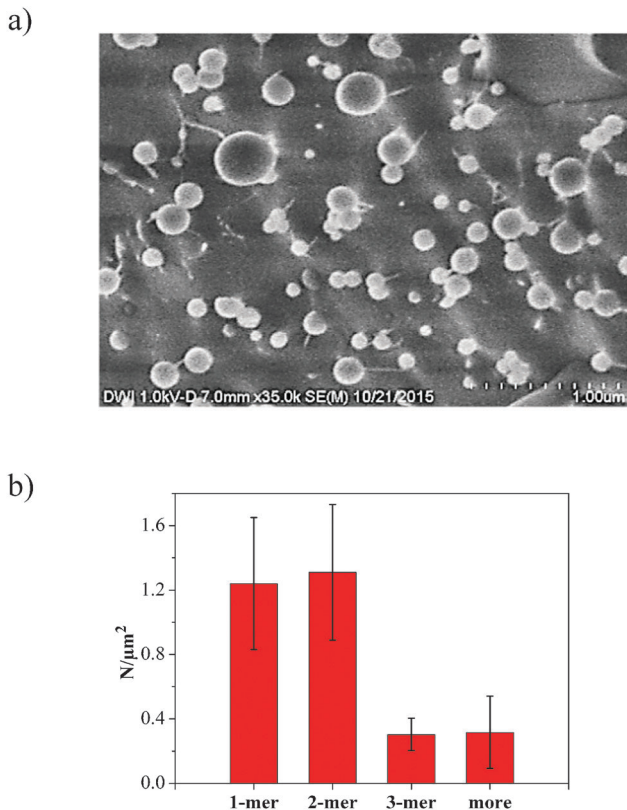
a)

b)

Fig. 2 (a) Cryo-FESEM micrograph, scale 1 μm of ELR microgels with a concentration of 10 mg mL^{-1} after 5 h incubation at 60 °C. (b) Statistics of the *i*-mers from cryo-FESEM micrographs.

at 60 °C for 5 h is shown in Fig. S1 (ESI†). The filaments indicated by the arrows are polypeptide fibrils attached to the ELR microgels. The thermally induced folding behavior of these filaments after irradiation with the electronic beam for several minutes (5–7 min) is shown at successive time intervals in Fig. S1a–f (ESI†).

Aggregation and volume phase temperature transition by DLS

Dynamic light scattering measurements give a *z*-average particle size or cumulant mean value and the polydispersity index (PDI) of the microgels.[43] The first-order correlation function of the electric field $g^{(1)}(t)$ detected by DLS can be analysed by the cumulant method and has the form:[43–45]

$$\ln\left|g^{(1)}(t)\right| = -\overline{\Gamma}t + \frac{1}{2!}\mu_2 t^2 - \frac{1}{3!}\mu_3 t^3 + \ldots, \quad (20)$$

where the background was subtracted, $\overline{\Gamma}$ is the average decay rate, and μ_2, μ_3, *etc.* represent the second, third, and higher moments about the mean. The polydispersity index is defined by PDI = $\mu_2/(2\overline{\Gamma}^2)$. From the first moment or mean decay rate $\overline{\Gamma}$ obtained from the linear slope of $\ln|g_1(t)|$ *versus* t, an intensity-weighted average of the diffusion coefficient or an effective diffusivity $\bar{D}$ can be calculated

$$\bar{D} = \frac{\overline{\Gamma}}{q^2} = \frac{\sum_i N_i(T)M_i^2 P_i(q, R_i(T))D_i(T)}{\sum_i N_i(T)M_i^2 P_i(q, R_i(T))}, \quad (21)$$

where $N_i(T)$ is the number of particles (aggregates) in class *i* at temperature T, M_i is the mass of the aggregate, the form factor $P_i(q, R_i(T))$ is a function of particle size R_i, and scattering vector q. The scattered intensity I_i of the *i*-fold aggregate can be expressed in terms of the form factor, *i.e.* $I_i(q) \propto M_i^2 P_i(q)$. The diffusivity D_i for aggregate *i* will depend on temperature due to the thermal activated collisions and volume phase temperature transition. Hence, eqn (21) describes the simultaneous effect of VPTT and aggregation processes due to the sensitivity to particle size.

Assuming the validity of the Stokes–Einstein equation we can define an effective hydrodynamic radius R_h of a collection of aggregates by

$$R_h = \frac{k_B T}{6\pi\eta\overline{D}}, \quad (22)$$

where k_B is the Boltzmann constant and η is the solvent viscosity. The dependence of the effective hydrodynamic radius R_h, measured by DLS as a function of temperature is shown in Fig. 3 for 2 mg mL^{-1} and 10 mg mL^{-1} concentration of ELR microgels. The main features of these dependences are: (i) the changes in the ELR microgel size in the heating stage (filled symbols in Fig. 3) are composed of an initial lag phase in which little or no aggregates are formed, followed by a growth phase that leads to the generation of dimers and high-order *i*-mers, and finally a plateau or saturation phase. (ii) Actually, during the lag period a small decrease in the value of the hydrodynamic radius takes place due to the volume phase temperature transition. This effect is more visible in the R_h distribution functions and the temperature dependence of the integral intensities of the ^{1}H HRMAS NMR spectra (see below). At larger temperatures the aggregation/disaggregation dominates the VPTT process. (iii) A hysteresis effect is revealed from the temperature evolution of the effective hydrodynamic radius in the heating and cooling periods (Fig. 3) that increases with the ELR microgel concentration.

A semiquantitative analysis of the effects of aggregation and VPTT processes on the ELR microgel effective hydrodynamic
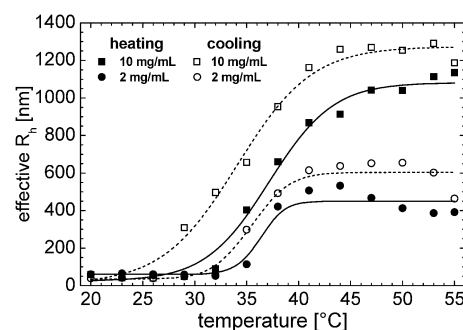

Fig. 3 The temperature dependence of the effective hydrodynamic radius R_h, measured by DLS for ELR microgels with 2 mg mL^{-1} and 10 mg mL^{-1} concentrations. The data for heating and cooling temperature changes are shown with filled and empty symbols, respectively. The incubation time between successive temperatures was 10 minutes. The fits by growing Boltzmann functions (eqn (23)) are shown by continuous and dashed lines, for heating and cooling, respectively.

radius measured by DLS can be made using the growing Boltzmann function

$$R_{\mathrm{h}}(T) = \frac{R_{\mathrm{h}}^{\mathrm{high}\,T} - R_{\mathrm{h}}^{\mathrm{low}\,T}}{1 + \exp\left\{-\dfrac{T - T_t}{\Delta T_t}\right\}} + R_{\mathrm{h}}^{\mathrm{low}\,T}, \qquad (23)$$

where T_t is the transition temperature, ΔT_t describes the width of the aggregation process, $R_{\mathrm{h}}^{\mathrm{low}\,T}$ and $R_{\mathrm{h}}^{\mathrm{high}\,T}$ are the plateaus at low and high temperatures, respectively, and from eqn (23) we can write $R_{\mathrm{h}}(T_t) = (R_{\mathrm{h}}^{\mathrm{high}\,T} + R_{\mathrm{h}}^{\mathrm{low}\,T})/2$. The growing sigmoidal shape data for the effective hydrodynamic radius shown in Fig. 3 were fitted with eqn (23) and the values of quantities T_t, ΔT_t, and $R_{\mathrm{h}}^{\mathrm{high}\,T}$ are shown in Fig. 4 for 2 mg mL^{-1} and 10 mg mL^{-1}
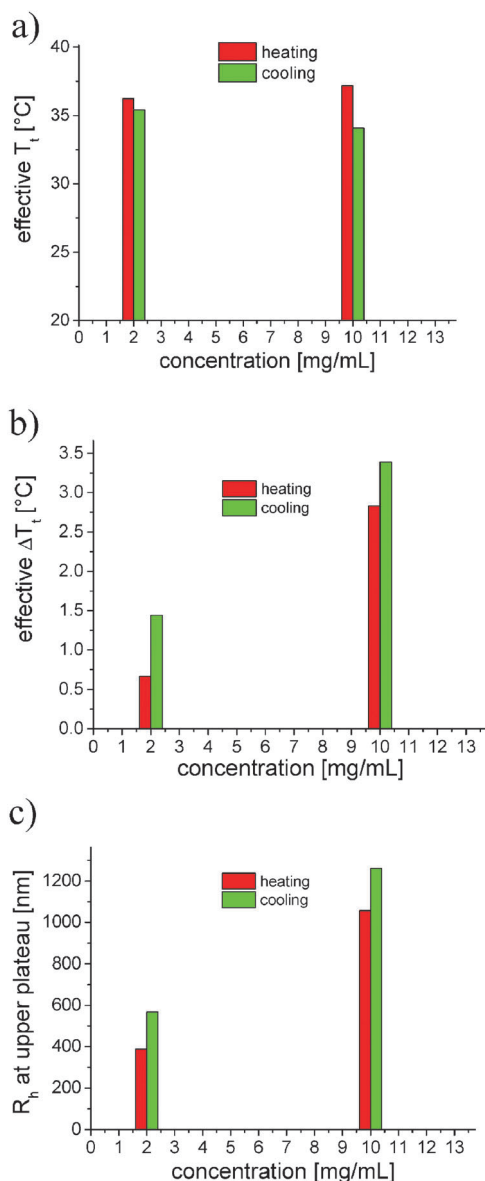

Fig. 4 Concentration dependence of the effective transition temperature T_t, (a), the effective transition width ΔT_t, (b), and the upper plateau effective hydrodynamic radius $R_{\mathrm{h}}^{\mathrm{high}\,T}$, (c) for ELR microgels with 2 mg mL^{-1} and 10 mg mL^{-1} concentrations in water.

concentrations of ELR microgels. The transition temperature T_t corresponds to the maximum slope of the $R_{\mathrm{h}}(T)$ function, i.e. for $\mathrm{d}^2(R_{\mathrm{h}}(T))/\mathrm{d}T^2 = 0$, and reflects more the aggregation process having different values for heating and cooling. The reaction rates for aggregation and disaggregation are different and the last process is faster compared to the former one, i.e. $T_t(\text{heating}) > T_t(\text{cooling})$ (Fig. 4a). The heterogeneity of the aggregation and disaggregation could be related to the effective width of transition ΔT_t (Fig. 4b). Large differences are detected between heating and cooling processes amplified by the increase in concentration. The quantity $R_{\mathrm{h}}^{\mathrm{high}\,T}$, which is the effective hydrodynamic radius at the upper plateau in Fig. 3 is shown in Fig. 4c. During the cooling process the plateau values of $R_{\mathrm{h}}^{\mathrm{high}\,T}$ obtained by Boltzmann function fits are larger compared with those of heating, this shows that at a given temperature the aggregates are more stable after they are produced.

The distribution functions for effective R_{h} evaluated from the analysis of the autocorrelation photon decays using the inverse Laplace transform algorithm are shown in Fig. 5. This is made from the DLS data for both ELR microgel concentrations and for heating and cooling temperature changes. In the temperature range of 20–29 °C and for heating and cooling temperature changes, the distributions have a larger width, revealing the competition effect of VPTT versus aggregation/disaggregation processes. The distribution becomes narrower in the temperature range of 41–55 °C where the aggregation/disaggregation processes dominate.

The dynamic light scattering data shown in Fig. 3 were measured using an incubation time of 10 minutes at each of the temperatures in the investigated range for both heating and cooling. In Fig. S2 (ESI†) the incubation time was increased to 45 minutes and the DLS data were taken at 20 °C, 30 °C, 40 °C, and 50 °C. The hysteresis effect of effective R_{h} is not diminished compared to that reported in Fig. 3 for 10 minute incubation time.

Proton high-resolution magic angle sample spinning (HRMAS) NMR spectra of ELR microgels

Proton HRMAS spectra giving access to hydrophilic and hydrophobic amino acids is possible in microgels due to fast rotation diffusion in the solvent that averages the dipolar interactions combined with sample rotation at the magic angle. This spectral resolution is partially affected by the magnetic susceptibility mismatch between the microgels and the solvent.

The proton HRMAS spectrum edited by spin echo in the aliphatic region of 0–4.6 ppm of the ELR microgels crosslinked by PEG-DGE with a molar ratio of 1 : 1 at 23 °C and a concentration of 10 mg mL^{-1} is shown in Fig. 6 and is similar to that reported in Fig. 2b of ref. 25 for a concentration of 2 mg mL^{-1}. The ^{1}H HRMAS spectrum reveals peaks of valine (Val-γCH$_3$), alanine (Ala-βCH$_2$), and proline (Pro-βCH$_2$).

The peak assignment in the HRMAS spectra shown in Fig. 6 was made by a combination of ^{1}H spectral simulation of individual amino acids in comparison to the ^{1}H spectra of two-synthetic elastin-like polypentapeptides, poly(G$_1$V$_1$G$_2$V$_2$P) and poly(AV$_1$GV$_2$P) reported in ref. 17. The recombinant elastin microgels were

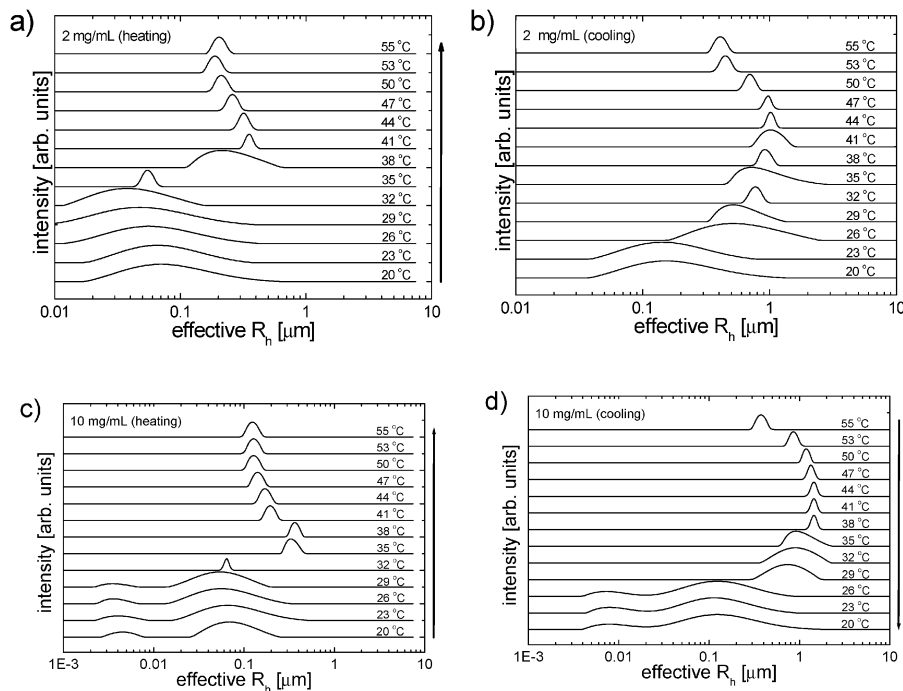**Fig. 5** Distribution functions of effective R_h for ELR microgels with 2 mg mL^{-1} ((a) and (b)) and 10 mg mL^{-1} ((c) and (d)) concentrations for heating and cooling changes of temperature. All the distributions were normalized to unity and are shown in a stack plot representation.
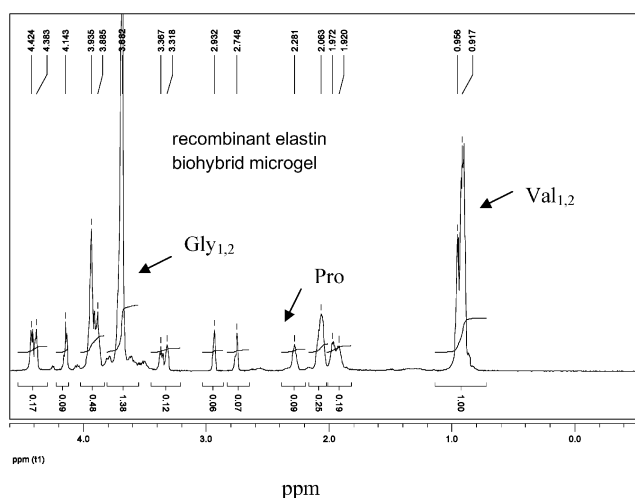

Fig. 6 Aliphatic region of the ^{1}H HRMAS spectrum edited by spin echo of ELR microgels with a concentration of 10 mg mL^{-1} measured in D$_2$O at 23 °C under sample rotation of 5 kHz. The side-chain peaks of glycine (α-CH$_2$), proline (β-CH$_2$), and valine (γ-CH$_3$) are marked by arrows. The polypeptides were crosslinked with PEG-DGE having a molar ratio of 1:1.

synthesized from model polypeptides MGKKKP[(VPGVG)$_{14}$]$_6$, where the essential amino acids used for our investigation are V = ʟ-valine, G = glycine, and P = ʟ-proline. The defined structure of recombinant microgels is reflected in sharp peaks of amino acids (Fig. 6). This is not the case for the native α-elastin where the structural heterogeneity leads to broad peaks especially in the glycine region.[10] Proton HRMAS spectra of ELR microgels reveal resolved peaks of hydrophobic valine

(Val-γCH$_3$) and proline (Pro-βCH$_2$). The glycine (Gly-αCH$_2$) peak is partially superimposed on the proline (Pro-αCH), and PEG (CH$_2$) peaks. However, the signals in the aliphatic region of Gly$_1$ and Gly$_2$ as well as Val$_1$ and Val$_2$ cannot be resolved under MAS conditions.[10,17,22]

Morphology and the effect of cross-link density of ELR microgels by ^{1}H transverse magnetization relaxation (T_2)

Proton transverse magnetization decays of microgels are sensitive to the core/corona morphology[46–48] or to the presence of hydrophobic and crosslinking domains like, as seen in the case of native α-elastin microgels.[10] In the last case the amino acid side chains in the hydrophobic domains have a larger amplitude and frequency of the segmental dynamics and hence a long transverse magnetization decay. The opposite situation is valid for the local segmental dynamics that are more restricted for the hydrophobic amino acids surrounding the crosslink points leading to biexponential decay. Normalized spin-echo decays of ELR microgels are measured for ELR microgels using spin echo and the associated HRMAS spectral integral intensities of the aliphatic region (0–4.6 ppm) are shown in Fig. S2 (ESI†).

The best fit of the spin-echo decays are obtained by a single-exponential function with the T_2 relaxation times shown in Fig. S3 (ESI†). This indicates that the mobility contrast between hydrophobic and crosslinking domains reduces in ELR microgels which are more organized in terms of polypeptide composition compared to native α-elastin microgels. The increase in the crosslink density reduces the segmental motions of oligopeptides[49] and the size of the microgel. Hence, T_2 relaxation time becomes shorter as is shown in Fig. S4 (ESI†).

The formation of dimers, trimers, and i-mers in the aggregation process affects the T_2 relaxation time and leads to the line broadening and finally to a reduction in NMR spectral intensity. Hence, not only the morphology of microgels can be investigated by transverse relaxation but also the aggregation and volume phase temperature transition (see below).[10,25]

Combined effect of volume phase temperature transition (VPTT) and aggregation process by ^{1}H HRMAS NMR spectral integral intensities of side-chain amino acids

In a recent work native, α-elastin hybrid microgel[9,10] showed VPTT which was determined by using the DLS technique. But for the concentration of 5 mg mL^{-1} and temperatures investigated no aggregation was detected in such microgels. The VPTT is also expected *a priori* to take place for ELR microgels but along with it, there is a simultaneous presence of aggregation. Below the transition temperature the biohybrid microgel is in a swollen state, given by the dissolution of the hydrophilic groups in water through the formation of hydrogen bonds. Above this temperature water is expelled from the microgel, the hydrophobic groups are free to interact, which leads to phase separation and collapse of the biopolymer and hence the microgel.

The swollen/deswollen process of microgels as well as aggregation can modify the side-chain mobility due to the changes in the microgel/aggregate segmental motions of the biopolymer network. These are directly reflected in the values of transverse relaxation time T_2 edited by spin echo and hence in the normalized integral intensities I/I_0 of the NMR peaks of the HRMAS spectra. In ref. 25 (Fig. 3) the spectral integral intensities were measured without the use of spin echo encoding but only by T_2 encoding during the spectrometer dead time of 5 μs. In the case of the VPTT process the temperature dependence of the ratio I/I_0 can be described by the phenomenological sigmoidal or decay Botzmann function

$$\frac{I}{I_0}(T) = \frac{a}{1 + \exp\left\{\dfrac{T - T_t}{\Delta T_t}\right\}} + b, \qquad (24)$$

where T_t is the transition temperature, ΔT_t describes the width of the VPTT, b is the plateau at large temperature and the a quantity is defined by $\dfrac{I}{I_0}(T_t) = \dfrac{a}{2} + b$. The above equation can be used where the aggregation and VPTT processes are simultaneously present like in the analysis made by DLS, where the growing Boltzmann function (eqn (23)) should be applied.

The temperature dependence of I/I_0 measured for ELR microgel with concentrations of 2 mg mL^{-1} and 10 mg mL^{-1} using ^{1}H HRMAS integral spectral intensity is shown in Fig. 7. The total integral intensity of the aliphatic region as well as that for valine and proline side-chain NMR peaks shows a decaying sigmoidal shape revealing that the aggregation process does not dominate the VPTT process (Fig. 7). Nevertheless, the temperature dependences of ELR microgels with 2 mg mL^{-1} and 10 mg mL^{-1} concentrations are different showing a larger aggregation for higher concentration. The effect of both processes is taken into account in this investigation by an effective transition temperature $T_{t,eff}$ and an effective transition width $\Delta T_{t,eff}$ obtained by fits with the Boltzmann function, eqn (24).
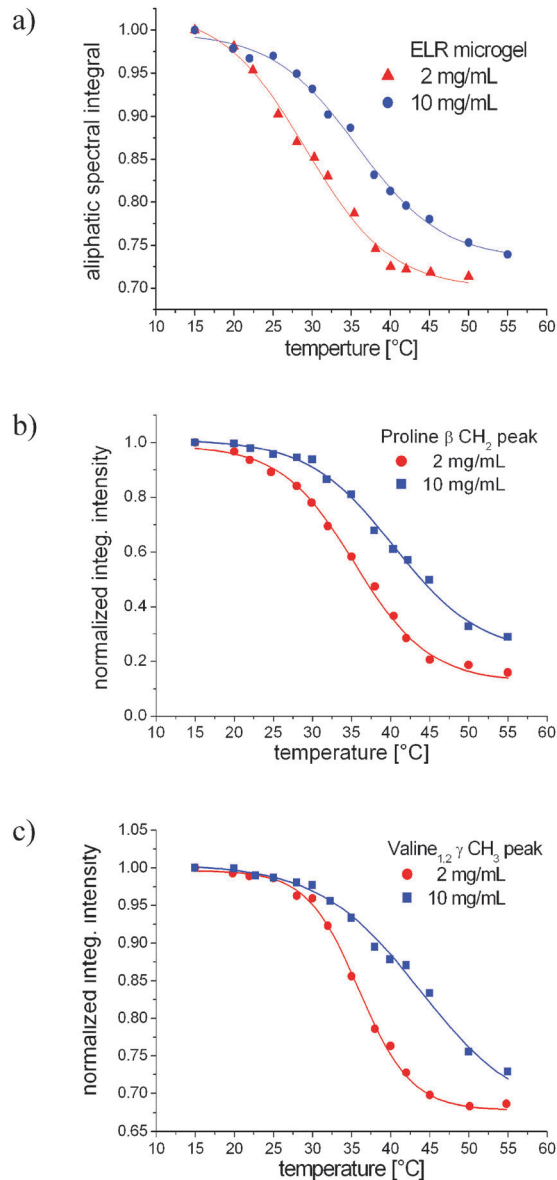
Fig. 7 The temperature dependences of the spectral integral of the aliphatic region (0–4.6 ppm) edited by spin-echo (a), and the normalized integral intensity of proline β CH$_2$ (b), and valine γ CH$_3$ (c) peaks from the ^{1}H HRMAS spectra of ELR microgels with concentrations of 2 mg mL^{-1} and 10 mg mL^{-1} in D$_2$O. The continuous lines are fits with the Boltzmann function (eqn (24)) and the fit parameters are reported in Tables 1 and 2.

The results are shown in Tables 1 and 2. The presence of aggregation at 10 mg mL^{-1} concentration is shown by the larger values of $T_{t,eff}$ compared to that for 2 mg mL^{-1} concentration (Table 1) for ELR microgels. The proline side-chains show larger temperature transition heterogeneity which is reflected in the values of $\Delta T_{t,eff}$ compared to that of Val that increases with ELR microgel concentration.

Aggregation of recombinant hybrid elastin microgels by concentration dependence of ^{1}H chemical shifts of amino acid side chains

Proton chemical shifts (δ) of the amino acid side chains measured by ^{1}H HRMAS NMR spectra edited by spin echo are

Table 1 The effective transition temperature ($T_{t,\text{eff}}$) and the effective transition width ($\Delta T_{t,\text{eff}}$) of the combined effect of volume phase temperature transition and aggregation of ELR microgels. These parameters are obtained by the fit of the data shown in Fig. 6 measured in the ^{1}H aliphatic region (0–4.6 ppm) of ELR with the Boltzmann function (eqn (24)). The microgels used have a 1:1 molar crosslink ratio of PEG-DGE at two concentrations in D$_2$O

$T_{t,\text{eff}}{}^a$ [°C] 2 mg mL^{-1}	$\Delta T_{t,\text{eff}}{}^a$ [°C] 2 mg mL^{-1}	$T_{t,\text{eff}}{}^a$ [°C] 10 mg mL^{-1}	$\Delta T_{t,\text{eff}}{}^a$ [°C] 10 mg mL^{-1}
29.2	5.3	35.7	5.4

^{a} The fit errors are of the order of 10%.

Table 2 The effective transition temperature ($T_{t,\text{eff}}$) and the effective transition width ($\Delta T_{t,\text{eff}}$) of the combined effect of volume phase temperature transition and aggregation of ELR microgels. These parameters are obtained by the fit of the data with the Boltzmann function eqn (24) and shown by continuous lines in Fig. 7b and c for proline and valine side chain spectra edited by spin echo. The microgels used have a 1:1 molar crosslink ratio of PEG-DGE at two concentrations in D$_2$O

Amino acid	$T_{t,\text{eff}}{}^a$ [°C] 2 mg mL^{-1}	$\Delta T_{t,\text{eff}}{}^a$ [°C] 2 mg mL^{-1}	$T_{t,\text{eff}}{}^a$ [°C] 10 mg mL^{-1}	$\Delta T_{t,\text{eff}}{}^a$ [°C] 10 mg mL^{-1}
Proline	35.3	4.8	40.2	5.4
Valine	35.8	3.3	43.4	6.3

^{a} The fit errors are of the order of 10%.

sensitive to the aggregation process of biohybrid microgels due to the changes in the conformations of polypeptides by the formation of aggregates. This is not a surface effect but occurs in the microgel volume as revealed by the amino acid side chain resonances having single-modal Lorenzian line shapes (Fig. 6). The values of the observed quantity δ_{obs} for Gly, Val, and Pro amino acids were measured for ELR microgels with a crosslinker molar mass ratio of 1:1 as a function of microgel concentration in D$_2$O. These dependences are shown in Fig. 8 for two temperatures 23 °C and 30 °C. The data were fit with eqn (11) and the fit parameters δ_{m}, δ_{d}, and K_{eff} are given in Table 3. For all side chains at both temperatures, the chemical shifts are shifted upfield with an increase in the ELR microgel concentration. This is a clear signature of the aggregation of ELR microgels due to the diamagnetic shielding of protons of amino acid side chains induced by aggregation.

The progressive changes in the ^{1}H HRMAS NMR spectrum with the microgel concentration at a fixed temperature is direct evidence of the aggregation and not of the VPTT process. This leads to the observation of a unique average signal whose chemical shift depends on species concentration and their respective chemical shifts. Thus, unimer–i-mer equilibrium is evident from the NMR spectrum.

Aggregation by the concentration dependence of the ELR microgel diffusivity. Translational self-diffusion of microgels can be accurately measured by NMR diffusometry using the Stejskal–Tanner approach based on the attenuation of the stimulated spin echo (STE) in the presence of variable pulsed field gradients.[50,51] For a given homogeneous family of molecules or aggregated microgels the dependence of the diffusivity D on the molecular mass M is given by[52]

$$D \propto M^{-\alpha}, \tag{25}$$

where the exponent α is related to the shape and fractal dimension of the diffusing micro-object and for spherical objects $\alpha = 1/3$. If the aggregation of microgels is taking place in the first approximation we can write from eqn (25) for the i-mer,

$$D(i) \propto M_i^{-\alpha_i} \tag{26}$$

Hence, the measurements of diffusivities for aggregated microgels can give information about the degree of aggregation, shape and fractal dimension of the aggregates.

The diffusivity was measured for two freshly prepared ELR microgels with concentrations of 2 mg mL^{-1} and 10 mg mL^{-1}. The stimulated echo decay is shown on a semi-logarithmic scale in the ESI,† Fig. S5a. In the limit of experimental errors only one self-diffusion coefficient was detected for each ELR microgel having values of D(2 mg mL^{-1}) = (4.64 ± 0.14) × 10^{-11} m^2 s^{-1} and D(10 mg mL^{-1}) = (4.59 ± 0.25) × 10^{-11} m^2 s^{-1} at 25 °C. Hence, it is justified to assume that the aggregates are not present in large amounts in the initial stage that is reflected in very close values for the diffusivities. Furthermore, the probability distributions of diffusivities (Fig. S5b, ESI†) show a small shift for the ELR microgels with a concentration of 10 mg mL^{-1} to a smaller value that can be interpreted as induced by the presence of aggregates, most probably dimers.

The diffusion coefficient was also measured for a series of ELR microgels with a concentration in the range of 2–8 mg mL^{-1} at 25 °C incubated for 11 h at 55 °C. All the diffusion decays are described by monoexponential functions that show that a fast equilibrium exchange takes place between monomers and dimers. The monoexponential fits are better than the biexponential but we mention that a Weibull function with a shape parameter β could be used to describe the diffusion decay in the presence of particle size distribution. Nevertheless, the presence of a new fit parameter will affect the accuracy of D coefficients. Fig. 9a shows the dependence of diffusivity as a function of ELR microgel concentration c, and was fitted by eqn (19). The fit parameters are $D_{\text{m}} = (6.96 ± 0.25) × 10^{-11}$ m^2 s^{-1}, $K_{\text{eff}} = (1.6 ± 0.3)$ mL mg^{-1} and $\lambda = 7.6 × 10^{-2}$ mL mg^{-1}. We can note that the effect of the reduction in the diffusivity due to particle crowding can be neglected in comparison to the aggregation ($\lambda \ll K_{\text{eff}}$). The normalized distributions obtained from inverse Laplace transform on diffusivity decays are shown in Fig. 9b. The trend in diffusivities is in good agreement with that obtained from the stimulated echo decays measured versus b quantity[51] and the D distribution width at half height for an ELR microgel concentration of 8 mg mL^{-1} is larger than that at 2 mg mL^{-1} microgel concentration. In the former case the sample is more heterogeneous compared to the lower concentration ELR microgel due to the presence of more ELR dimer microgels coexisting with the unimers. We can mention that the time windows of the DLS and NMR diffusometry are different that leads to differences in the distribution widths of R_{h} and D (compare Fig. 5 and 9b).

The diffusivity of the dimers can be correlated with the aspect ratio $p = L/d$. In the approximation of a cylinder-shape dimer L and d are the length and diameter of the cylinder, respectively. These quantities can be approximated by the cryo-TEM micrograph presented in Fig. 1b for ELR microgel from
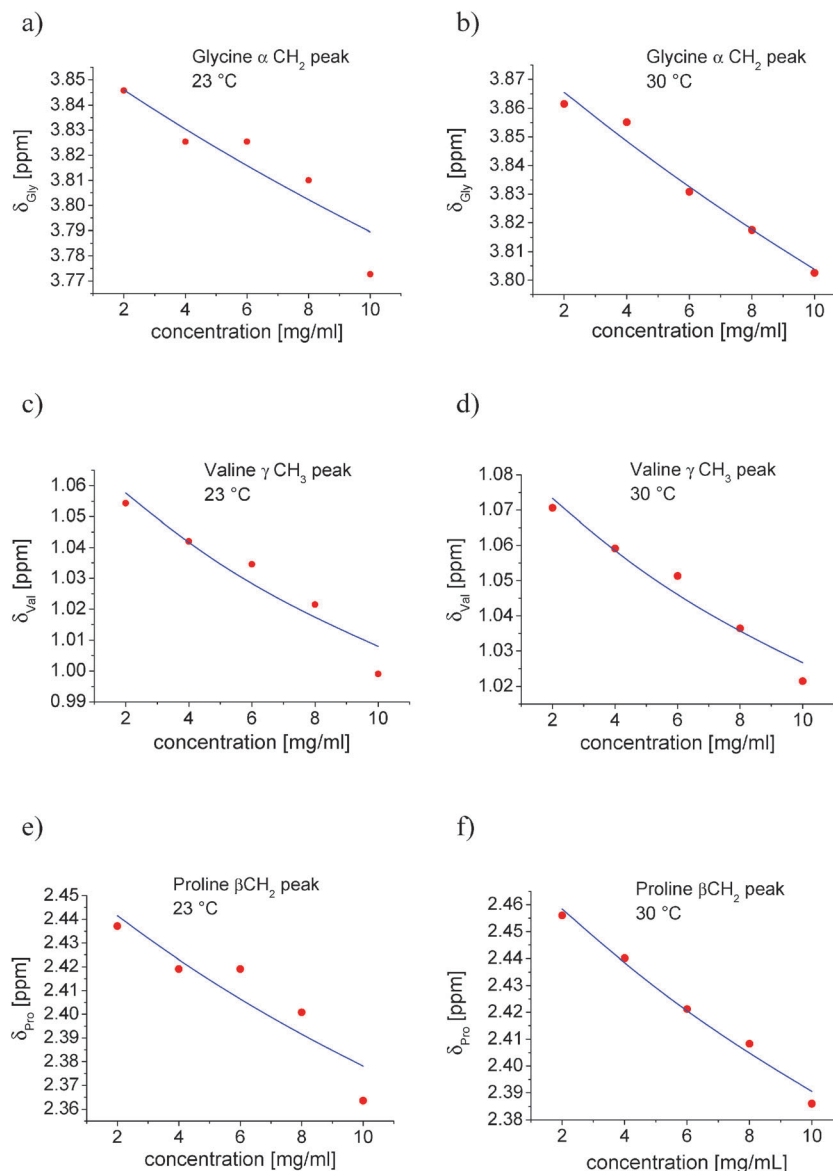
Fig. 8 The dependence of the ^{1}H chemical shifts of the amino acid side chains on the concentration of ELR microgels in D$_2$O measured at 23 °C and 30 °C. The errors in the values of chemical shifts are of the order of 2%. The continuous lines are fits (average $\chi^2 \approx 0.0004$ and $R^2 \approx 0.959$) based on eqn (11) and the fit parameters are given in Table 3 for Gly, Pro, and Val amino acids.

Table 3 Characterization of ELR microgel aggregation by concentration dependence of amino acid side chain ^{1}H chemical shifts. The fit parameters δ_m, δ_d, and K_{eff} were obtained from eqn (11)

Temperature	Amino acid	δ_m [ppm]	δ_d [ppm]	Average K_{eff} [mL mg^{-1}]
23 °C	Glycine	3.95	3.20	
	Proline	2.45	1.88	8.2
	Valine	1.92	0.80	
30 °C	Glycine	3.96	3.30	
	Proline	2.47	1.92	9.1
	Valine	1.94	0.82	

which the aspect ratio is $p = 1.82$. Eqn (15) and (16) allow us to evaluate the diffusivity of the dimers from which we finally get $D_d \approx 4.0 \times 10^{-11}$ m^2 s^{-1} that is in a good agreement with the values of D_d obtained from eqn (14) and the value of D_m obtained from the concentration dependence shown in Fig. 9a.

We can mention at this point the differences in the sizes of ELR microgels measured by various analytical methods. Using cryo-TEM micrographs at a concentration of 10 mg mL^{-1} ELR microgel, the average unimer diameter can be evaluated from Fig. 1a to be ~ 250 nm. From DLS in the approximation of the effective hydrodynamic radius (Fig. 5c) at 25 °C we obtain the diameter ($2R_{eff}$) of ~ 120 nm. Hence, there is only an order of magnitude agreement between these two methods. Furthermore, it is well known that Inverse Laplace Transform used in DLS for generating the R_{eff} distribution is affected by numerical artefacts.[51] We assume that the broad peak in Fig. 5c and d situated below 10 nm is such an artefact. Furthermore, the evaluation of the

a)

b)
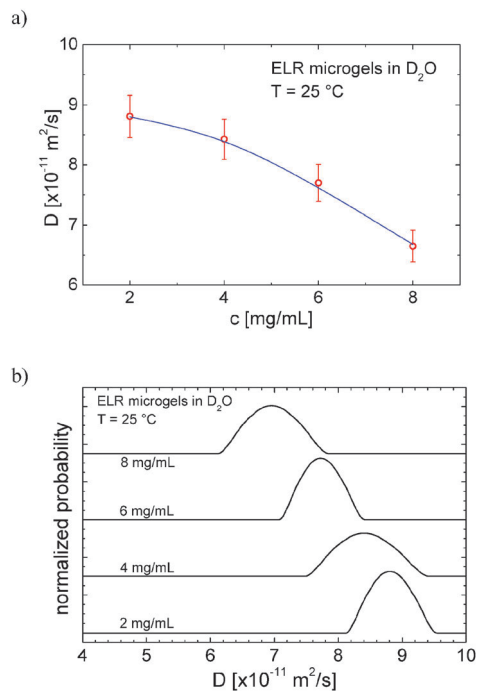
Fig. 9 (a) The dependence of the diffusivity of ELR microgels in D_2O at 25 °C as a function of microgel concentration measured from pulsed field gradient stimulated echo decays. The continuous line shows the fit ($\chi^2 \approx$ 0.0017 and $R^2 \approx$ 0.999) with eqn (19) and the free parameter values are reported in the text. (b) Normalized diffusivity distributions for the series of ELR microgels with different concentrations obtained by inverse Laplace transform from stimulated echo decays in the Stejskal–Tanner experiments.[27]

hydrodynamic radius from diffusivity NMR measurement is difficult to be made due to the factal nature of ELR microgels and the presence of elongated dimers.

Conclusions

In this work we investigated the aggregation behavior of the ELR microgels. The dependence of this process as a function of the microgel concentrations and temperature was studied by different analytical methods. Upon heating and cooling, the ELR microgels showed a hysteresis effect which was measured by DLS. This ascertains the dependence of the degree of aggregation on microgel concentration.

The aggregation and the hysteresis effect were detected only for the ELR microgels and not for native α-elastin microgels, with a concentration comparable to the concentrations used in this study.[9,10] This is related to the differences in the amino-acid architecture of the microgels that leads to new structure–property relationships. But still it is preliminary to speculate at this moment on the molecular interactions, which leads to the differences in the aggregation behavior of the two elastin microgels.

The distribution functions of the effective hydrodynamic radius measured by DLS reveals an interplay of thermo-responsiveness and aggregation of ELR microgels. The temperature dependence of the photon autocorrelation function is

dominated by the aggregation process due to large changes in the particle sizes. Due to the presence of hydrophobic and hydrophilic amino acid side chains in the microgel architecture VPTT along with aggregation was also detected by ^{1}H HRMAS NMR. The efficiency of these two processes is directly related to the strength of the water–segmental, segmental–segmental, intra-microgel and inter-microgel interactions, which are dominated by the hydrophobic domains. One possibility of separating these effects by studying the changes in the microgel size or NMR parameters at fixed temperature as a function of particle concentration. Another possibility was to detect by ^{1}H HRMAS NMR spectroscopy the ^{1}H chemical shifts of hydrophobic and hydrophilic amino acid side chains having homogenous resonances. The result shows that the process of ELR microgel aggregation not only affects the surface of microgels, but also their entire volume. Furthermore, the presence of aggregation for ELR microgels was proved by the measurements of the self-diffusion coefficients as a function of concentration at constant temperature. Under such conditions the aggregation can be investigated separately from the VPTT process. The population balance kinetic and isodesmic aggregation models describe in the good approximation the concentration dependence of the hydrodynamic radius and microgel diffusivities.

Understanding the complex behaviour of ELR microgels in the process of coacervation–decoacervation and the temperature response may be useful for the design and understanding of other thermally responsive biohybrid microgels for diverse applications in nanomedicine.

Acknowledgements

Notes and references

1 L. Cademartiri and K. J. M. Bishop, *Nat. Mater.*, 2015, **14**, 2–9.
2 S. Chen and A. S. Hoffman, *Macromol. Rapid Commun.*, 1995, **16**, 175–182.
3 D. E. Bergbreiter, B. L. Case, Y. S. Liu and C. W. Caraway, *Macromolecules*, 1998, **31**, 6053–6062.
4 B. R. Saunders, N. Laajam, E. Daly, S. Teow, X. H. Hu and R. Stepto, *Adv. Colloid Interface Sci.*, 2009, **147**, 251–262.
5 F. G. Quiroz and A. Chilkoti, *Nat. Mater.*, 2015, **14**, 1164–1171.
6 S. Singh, M. Möller and A. Pich, *J. Polym. Sci., Part A: Polym. Chem.*, 2013, **51**, 3044–3057.

7 J. K. Oh, R. Drumright, D. J. Siegwart and K. Matyjaszewski, *Prog. Polym. Sci.*, 2008, **33**, 448–477.

8 A. V. Kabanov and S. V. Vinogradov, *Angew. Chem., Int. Ed.*, 2009, **48**, 5418–5429.

9 S. Singh, F. Topuz, K. Albrecht, J. Groll and M. Möller, *Adv. Polym. Sci.*, 2013, **12**, 268–287.

10 A. Balaceanu, S. Singh, D. E. Demco and M. Möller, *Chem. Phys. Lett.*, 2014, **612**, 182–189.

11 F. Chiti, P. Webster, N. Taddei, A. Clark, M. Stefani, G. Ramponi and C. M. Dobson, *Proc. Natl. Acad. Sci. U. S. A.*, 1999, **96**, 3590–3594.

12 P. Arosio, S. Rima, M. Lattuada and M. J. Morbidelli, *J. Phys. Chem. B*, 2012, **116**, 7066–7075.

13 W. Wang, *Int. J. Pharm.*, 2005, **289**, 1–9.

14 D. W. Urry, *J. Protein Chem.*, 1988, **7**, 1–34.

15 B. Vrhovski, S. Jensen and A. S. Weiss, *Eur. J. Biochem.*, 1997, **250**, 92–98.

16 C. M. Bellingham and F. W. Keely, *Curr. Opin. Solid State Mater. Sci.*, 2004, **8**, 135–139.

17 D. Kurkova, J. Kriz, P. Schmidt, J. Dybal, J. C. Rodriguez-Cabello and M. Alonso, *Biomacromolecules*, 2003, **4**, 589–601.

18 B. Frohm, J. E. DeNizio, D. S. M. Lee, L. Gentile, U. Olsson, J. Malm, K. S. Akerfeldt and S. Linse, *Soft Matter*, 2015, **11**, 414–421.

19 J. R. McDaniel, J. Bhattacharyya, K. B. Vargo, W. Hassouneh, D. A. Hammer and A. Chilkoti, *Angew. Chem., Int. Ed.*, 2013, **52**, 1683–1687.

20 I. González de Torre, L. Quintanilla, G. Pinedo-Martín, M. Alonso and J. C. Rodríguez-Cabello, *ACS Appl. Mater. Interfaces*, 2014, **6**, 14509–14515.

21 D. H. T. Le, R. Hanamura, D.-H. Pham, M. Kato, D. A. Tirrell, T. Okubo and A. Sugawara-Narutaki, *Biomacromolecules*, 2013, **14**, 1028–1032.

22 F. Zhao, Y. Zhao, Y. Liu, X. Chang, C. Chen and Y. Zhao, *Small*, 2011, **7**, 1322–1337.

23 D. W. Urry, *J. Phys. Chem. B*, 1997, **101**, 11007–11028.

24 I. Gonsáles de Torre, M. Santos, L. Quintanilla, A. Teresa, M. Alonso and J. C. Rodríguez-Cabello, *Acta Biomater.*, 2014, **10**, 2495–2505.

25 S. Singh, D. E. Demco, K. Rahimi, R. Fechete, J. C. Radriguez-Cabello and M. Möller, *Macromol. Rapid Commun.*, 2015, **37**, 181–186.

26 M. Pierna, M. Santos, F. J. Arias, M. Alonso and J. C. Rodríguez-Cabello, *Biomacromolecules*, 2013, **14**, 1893–1903.

27 E. O. Stejskal and J. E. Tanner, *J. Chem. Phys.*, 1965, **42**, 288–292.

28 C. J. Roberts, *J. Phys. Chem. B*, 2003, **107**, 1194–1207.

29 V. Fodera, A. Zaccone, M. Lattuada and A. M. Donald, *Phys. Rev. Lett.*, 2013, **111**, 108105.

30 R. B. Martin, *Chem. Rev.*, 1996, **96**, 3043–3064.

31 R. Ferrazza, B. Rosi and G. Guella, *J. Phys. Chem. B*, 2014, **118**, 7147–7155.

32 M. Majer and K. Zick, *J. Chem. Phys.*, 2015, **142**, 164202–164207.

33 R. M. Venable and R. W. Pastor, *Biopolymers*, 1988, **27**, 1001–1014.

34 J. Garcia de la Torre and N. A. Bloomfield, *Q. Rev. Biophys.*, 1981, **14**, 81–139.

35 V. V. Krishnan, *J. Magn. Reson.*, 1997, **124**, 468–473.

36 A. Orteg and J. Garcia de la Torre, *J. Chem. Phys.*, 2003, **119**, 9914–9919.

37 M. Tirado, M. López Martinez and J. Garcia de la Torre, *J. Chem. Phys.*, 1984, **81**, 2047–2053.

38 H.-X. Zhou, *Biophys. J.*, 1995, **69**, 2286–2297.

39 W. S. Price, F. Tsuchiya and Y. Arata, *J. Am. Chem. Soc.*, 1999, **121**, 11503–11512.

40 J. Han and J. Herzfeld, *Biophys. J.*, 1993, **65**, 1155–1161.

41 M. Tokuyama and I. Oppenheim, *Phys. Rev. E: Stat. Phys., Plasmas, Fluids, Relat. Interdisc. Top.*, 1994, **50**, R16–R19.

42 P. R. Wills and Y. Georgalls, *J. Phys. Chem.*, 1981, **85**, 3978–3984.

43 P. Hassan, S. Rana and G. Verma, *Langmuir*, 2015, **31**, 3–12.

44 H. Holthof, S. F. Egelhaaf, M. Borkovec, P. Schurtenberger and H. Sticher, *Langmuir*, 1996, **12**, 5541–5549.

45 M. R. Dreher, A. J. Simnick, K. Fisher, R. J. Smith, A. Patel, M. Schmidt and A. Chilkoti, *J. Am. Chem. Soc.*, 2008, **130**, 687–694.

46 A. Balaceanu, D. E. Demco, M. Möller and A. Pich, *Macromolecules*, 2011, **44**, 2161–2169.

47 A. Balaceanu, D. E. Demco, M. Möller and A. Pich, *Macromol. Chem. Phys.*, 2011, **212**, 2467–2477.

48 A. Balaceanu, D. E. Demco, M. Möller and A. Pich, *Macromolecules*, 2013, **46**, 4882–4891.

49 P. Sotta, C. Fülber, D. E. Demco, B. Blümich and H. W. Spiess, *Macromolecules*, 1996, **29**, 6222–6230.

50 Y. E. Shapiro, *Prog. Polym. Sci.*, 2011, **36**, 1184–1253.

51 P. T. Callaghan, *Principles of Nuclear Magnetic Resonance Microscopy*, Oxford University Press, New York, 1991.

52 A. Augé, P.-O. Schmit, C. A. Crutchfield, M. T. Islam, D. J. Harris, E. Durand, M. Clemancy, A.-A. Quoineaud, J.-M. Lancelin, Y. Prigent, F. Taulelle and M.-A. Delsuc, *J. Phys. Chem. B*, 2009, **113**, 1914–1918.